Nanoscale

COMMUNICATION

View Article Online
View Journal | View Issue

Cite this: *Nanoscale*, 2025, **17**, 19127

Received 30th May 2025,
Accepted 28th July 2025

DOI: 10.1039/d5nr02285a

rsc.li/nanoscale

Multifunctional microring structures enabled by SiN for advanced optically pumped atomic technologies

Xiaoqin Meng,[a,b,c,d,e] Zhen Chai, *[a,b,c,d,e] Yuting Xu,[a,b,c,d,e] Ye Tong,[a,b,c,d,e] Jie Sun,[a,b,c,d,e] Xinran Su[a,b,c,d,e] and Xuelei Wang[c,e]

As quantum technology advances, integrated optical chips demonstrate extensive potential in quantum information processing, atomic system measurements, and precision sensing. This paper introduces a design for a highly integrated, robust, and easily fabricated multifunctional silicon nitride (SiN) array microring chip emitter for optically pumped atomic systems. The chip emits uniformly distributed circularly polarized light at 795 nm and vortex light at 778.1 nm (l = 3) with vertical radiation. Experimental results align closely with theoretical calculations. This device is anticipated to simultaneously achieve optical pumping of polarized atoms and laser frequency stabilization in atomic systems, offering a significant direction for developing chip-scale optical emitters in quantum applications. It holds the potential to play a crucial role in atomic clocks, quantum communication, and quantum sensing.

1. Introduction

Devices based on alkali metal atomic vapor cells can measure various physical parameters, such as magnetic fields,[1,2] rotational angular velocity,[3] and time.[4] With advancements in microfabrication technology, chip-scale atomic systems utilizing light–atom interactions have significantly reduced the size and power consumption required for quantum metrology applications. However, most atomic systems rely on bulk optical components and suffer from constrained miniaturization and increased costs. Integrating some or all optical components onto a single photonic chip effectively addresses these challenges. Concurrently, silicon nitride (SiN) photonic platforms offer substantial improvements in integration and compactness. SiN is an important optical waveguide material due to its broad transparency range (400–2350 nm).[5] It is extensively used with atomic and molecular vapors and can integrate directly with other SiN photonic devices.[6,7] In recent years, numerous applications in integrated photonics have utilized SiN waveguide structures to emit guided modes to customize free-space propagating beams. There are three primary methods to achieve this. One is grating-structured radiation of guided modes, which has increasingly more applications in ion-trapping quantum systems[8,9] and devices based on atomic vapor spectroscopy. These devices feature extremely compact packaging (<1 cm^3),[10–12] high stability, and strong robustness. However, due to fabrication imperfections, such approaches require active phase tuning, and the purity of the emitted circularly polarized light (CPL) is limited.[13,14] Waveguide-driven metasurface far-field radiation can simultaneously control the amplitude, phase, and polarization of far-field radiation. However, its manufacturing involves precise nanostructures and waveguide integration, resulting in low robustness and requiring complex processes and precise control.[15,16] Unlike the two methods mentioned above, using a ring resonator as a beam generator has garnered significant attention from researchers. The ring resonator can be scaled to tens of microns and allows for continuous modulation of orbital angular momentum (OAM) eigenstates by tuning the incident wavelength.[17] Additionally, it ensures high circular polarization purity emission at the maximum intensity of the emitted beam.[18] The Purcell effect enhanced by resonant cavity restricts the emitted light to a specific polarization mode, meeting the requirements of harsh scenarios such as polarized atoms.

This study presents a passive waveguide-based microring resonator emission system designed for precise measurements in atomic systems. By adjusting the incident wavelength, the microring chip can emit light at two distinct wavelengths. At 795 nm, it produces a highly circularly polarized beam with a state of polarization (SOP) exceeding 93.5%. The experimental

[a]*Key Laboratory of Ultra-Weak Magnetic Field Measurement Technology, Ministry of Education, School of Instrumentation and Optoelectronic Engineering, Beihang University, Beijing, 100191, China. E-mail: zhenchai@buaa.edu.cn*
[b]*Institute of Large-Scale Scientific Facility and Centre for Zero Magnetic Field Science, Beihang University, Beijing 100191, China*
[c]*Hangzhou Extremely Weak Magnetic Field National Key Science and Technology Infrastructure Research Institute, Hangzhou 310051, Zhejiang, China*
[d]*Beihang Hangzhou Innovation Institute, Hangzhou 310052, Zhejiang, China*
[e]*Hefei National Laboratory, Hefei 230088, Anhui, China*

findings closely align with theoretical simulations. This beam facilitates high-precision spectroscopy and atomic ensemble polarization. At 778.1 nm, the chip generates l = 3 vortex beams with consistent performance, supporting frequency stabilization and spectroscopic applications in atomic systems. The emitter utilizes an integrated optical platform, ensuring the on-chip optical system robustness and simplifying the fabrication process. Through an optimized optical design and structure, the chip achieves the desired emissions with reduced design complexity.

2. Design of microring emitter

In atomic systems, CPL can selectively excite alkali metal atoms, inducing photon absorption transitions to specific energy levels [Fig. 1(c)]. For instance, in ^{87}Rb atoms, the alkali metal atoms resonate with incident light and absorb photons at 795 nm or 780 nm in their ground state $5^2S_{1/2}$, transitioning to the excited states of $5^2P_{1/2}$ or $5^2P_{3/2}$. This single-photon absorption process, combined with spin-exchange collisions, polarizes the ensemble of alkali metal atoms. This process has found widespread applications in atomic magnetometers,[2] atomic clocks,[19] and atomic inertial measurements.[20] Under pump light influence, Rb atoms can simultaneously absorb two photons at 778.1 nm, transitioning from the ground state $5^2S_{1/2}$ to the pump upper energy level $5^2D_{5/2}$. This process initiates four-wave mixing, generating coherent visible blue light and mid-infrared lasers. These properties prove valuable for applications such as atomic clocks,[21,22] high-resolution spectroscopy,[23] and laser frequency stabilization[24] [Fig. 1(a)].

The overall configuration of beam emission from the waveguide microring resonators is illustrated in Fig. 1(b). The device, measuring 4.0 mm × 3.5 mm, comprises SiN waveguides on a Si substrate. The waveguides possess cross-sectional dimensions of 500 nm in width and 250 nm in height, fully etched and encased in SiO_2 layers approximately 2 μm thick, as depicted in Fig. 2(a)–(c). The chip utilizes an inverted-tapered coupler to facilitate light coupling from external optical fibers or lasers into the SiN waveguides. The multi-mode interference (MMI) structure divides the light within the waveguide and directs it to the microring array emitters, which radiate the beam vertically upward into the cell. The microring resonator supports whispering gallery modes (WGMs) with high OAM.[17,18] Grating structures etched inside the microring resonator enable the extraction and emission of confined microwave signals into free space with a 452 nm period and a 30% duty cycle [Fig. 2(b)]. The angular grating within the microring functions analogously to a grating coupler in straight waveguides.[8] As guided waves scatter through the grating elements, a portion of the power is directed in the ϕ direction, generating a tilted wavefront at an emission angle ϕ. The circular symmetry of the microring facilitates the formation of the WGMs, which resonate according to eqn (1):

$$2\pi R n_{\text{eff}} = m\lambda \tag{1}$$

where R represents the effective radius of the microring, n_{eff} denotes the effective refractive index, m signifies the azimuthal

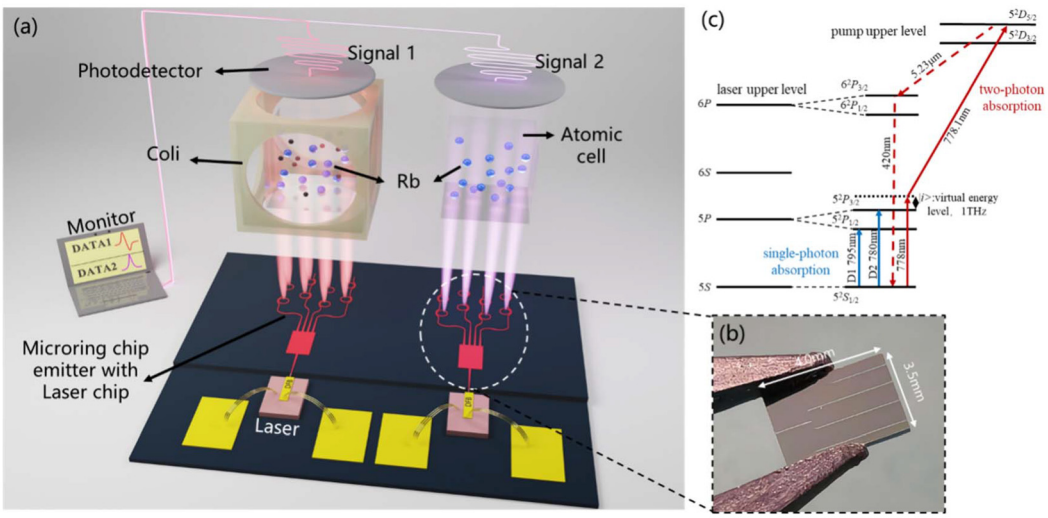

Fig. 1 (a) Diagram of a microring chip based on SiN waveguide designed for optically pumped atomic systems. The chip emitter based on microring structure is heterogeneously integrated with the laser chip, with metal layers on both sides to provide current, ensuring stable light output and supplying power to the SiN optical path. The system's sensitive component, a rubidium vapor cell, is encircled by magnetic compensation and modulation coils and positioned within a magnetically shielded environment (not depicted). A photodetector (PD) mounted atop the cell interfaces with external devices for data processing and frequency stabilization. The red beams exhibit a wavelength of 795 nm, while the purple beams correspond to 778.1 nm. The light enters the waveguide, divides through a multi-mode interference (MMI) structure, traverses the microring array, and subsequently emits vertically into the cell to polarize the atoms; (b) image of the microring array chip emitter; (c) energy level transitions for single-photon absorption and two-photon absorption (2PA) in ^{87}Rb atoms, with blue arrows representing single-photon absorption transitions and red arrows indicating 2PA transitions.

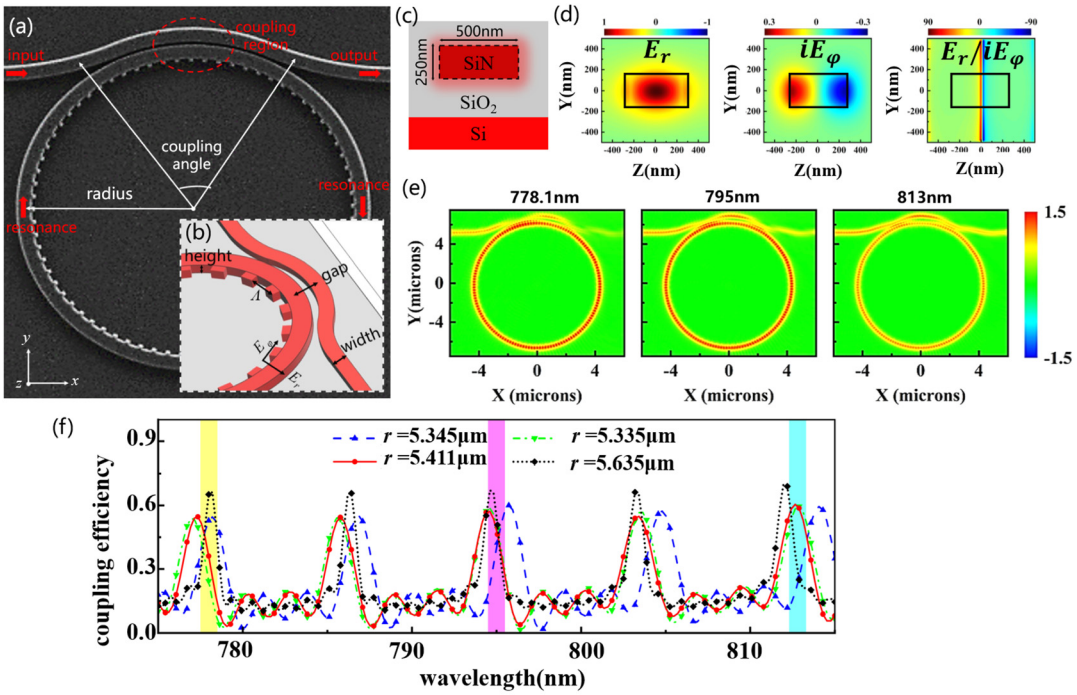

Fig. 2 Simulation design of silicon nitride microring emitter. (a) SEM image of the fabricated device (R = 5.41 μm); (b) diagram of the internal grating amplification structure within the microring, with a grating period Λ of approximately 452 nm and a duty cycle of 30%; (c) the cross-sectional schematic of the waveguide, featuring a SiN core with a thickness of 250 nm, cladded on both sides with 1 μm thick layers of SiO_2; (d) the figures show the radial component E_r, azimuthal component iE_φ, and component duty ratio E_r/iE_φ of the fundamental quasi-transverse electric (TE) mode in the SiN waveguide, shown from left to right; (e) internal field distribution during microring transmission at different wavelengths; (f) radiation spectra of the microring device with varying radii.

mode number or resonator mode number, and λ indicates the free-space wavelength. The angular grating within the microring introduces perturbations, resulting in gradual amplitude variations. When the Bragg equation is satisfied, light in the microring scatters due to the angular grating.[12] The Bragg equation is as follows:

$$\beta R - \nu_{\mathrm{rad}} = nKR \quad n = \pm 1, \pm 2, \ldots \tag{2}$$

where ν_{rad} represents the angular propagation constant of the radiation beam, indicating the phase change per unit angle. The parameter KR denotes the number of periods of the angular grating or the number of gratings q around the microring resonator. $K = 2\pi/\Lambda$ is defined as the grating spatial frequency, where Λ represents the grating period. $\beta R = 2\pi n_{\mathrm{eff}} R/\lambda$ corresponds to the azimuthal order p of the WGMs involved or the number of optical periods around the microring resonator. The angular phase-matching condition is expressed by eqn (3):[25]

$$\nu_{\mathrm{rad}} = p - q \tag{3}$$

For a single device, q represents the structural constant, while the value of p can be adjusted by activating specific WGMs.

Fig. 2(d) illustrates the simulated cross-sectional electric field distribution of the fundamental TE mode in the SiN waveguide (indicated by the black line). At the wavelength of 795 nm, the effective refractive index is n_{eff} = 1.70 for the TE mode and n_{eff} = 1.645 for the transverse magnetic (TM) mode. With a $\pm\pi/2$ phase shift relative to E_r, a pronounced azimuthal component iE_φ is also observable at the transverse cladding interface (sidewalls). Due to the symmetry of the microring and grating structures, the radiated beam maintains a cylindrical beam profile.[18] In this device, the optical field inside the microring initially propagates mainly along the radial polarization. Due to disturbances caused by the internal grating period, the light inside the microring radiates with an angular orientation. In the paraxial limit, the eigenmodes in this basis would correspond to the Laguerre–Gauss modes. Radial polarized radiation with azimuthal phase factor $e^{il\phi}$ can be written as:

$$E_{\mathrm{r}} = \frac{E_0}{\sqrt{2}}(\hat{\sigma}_+ e^{i(l-1)\phi} + \hat{\sigma}_- e^{i(l+1)\phi}) \tag{4}$$

As per eqn (4), only those modes with a zero azimuthal phase factor exhibit non-zero intensity on axis, attributable to the phase singularity.[18] Consequently, for a topological charge of l = 1, only right-hand circular polarization (RHCP) beams propagate on axis, whereas for l = −1, only left-hand circular polarization (LHCP) beams are emitted. The designed microring chip emitter operates at wavelengths corresponding to the single-photon absorption D1 line of Rb atoms (795 nm) and two-photon absorption (2PA, 778.1 nm). The radiated beams

exhibit topological charges of $l_{795\ nm} = 1$ and $l_{778.1\ nm} = 3$, respectively. Fig. 2(a) presents the scanning electron microscope (SEM) image of the microring device with a radius (R) of 5.41 μm. Grating structures are etched inside the microring resonator, with $q = 72$ [Fig. 2(b)]. The first-order diffraction wavelength of the microring spans from 640 to 1300 nm, with an approximate spacing of ~8.14 nm between adjacent resonant wavelengths.

Utilizing three-dimensional finite-difference time-domain (FDTD) simulations, we ascertained that the azimuthal order of the microring resonator at 795 nm was $p = 73$. Fig. 2(e) illustrates the internal transmission distribution within the microring. The results indicate that during transmission at different wavelengths, most of the light is coupled into the microring and generates resonance. Based on the previous formulas, the theoretical range of the microring radius for different orders is initially calculated. To meet the polarization requirements of ^{87}Rb atoms, the theoretical radius range is optimized in the FDTD simulation. The final result is presented in the spectrum shown in Fig. 2(f). Different filling colors correspond to the near-field distributions of radiation at different wavelengths shown in Fig. 2(e). When R = 5.411 μm, at the resonance wavelength of 795 nm, the radiation beam exhibits non-zero intensity at the center, and the radiation spot order $l = 1$. As the absolute value of l increases, the central singularity (zero-intensity region) expands proportionally. We further simulated and calculated in the region of non-zero intensity at the center (SI). The polarization state of the central spot is predominantly RHCP, with SOP exceeding 99%.[18]

3. Experimental results of the chip

The performance characterization of the chip's radiated optical field was conducted using a manual coupling system experimental setup, with the results presented in Fig. 3. Fig. 3(a) presents a comparison between the simulated (left) and the actual measured far-field distribution captured by a complementary metal–oxide–semiconductor transistor (CMOS) camera (right). For $l = 1$, we observe non-zero intensity at the center. The simulated mode closely aligns with the measured output, exhibiting a divergence angle of approximately 4°. For $l = 3$, the overall characteristics align, exhibiting a singularity where the optical field is zero. We subsequently incorporated a quarter-wave plate (QWP), half-wave plate (HWP), and polarizing beam splitter (PBS) into the optical path. Employing the method described in ref. 26, we measured the Stokes parameters of the radiated beam (SI: additional experimental details and results). After eliminating interference from surrounding stray light, the Stokes parameters reveal that the majority of the light is in the S3 (RHCP), indicating that the radiated beam is predominantly RHCP [Fig. 3(b)]. The calculated SOP is approximately 93.5%, which aligns well with the previous results.

In our previous work,[27] we utilized the manual coupling system to achieve high-precision alignment and coupling between the optical fiber and the chip edge by adjusting a five-axis displacement table. Meanwhile, an objective lens and a camera were used above the chip to detect the diffraction

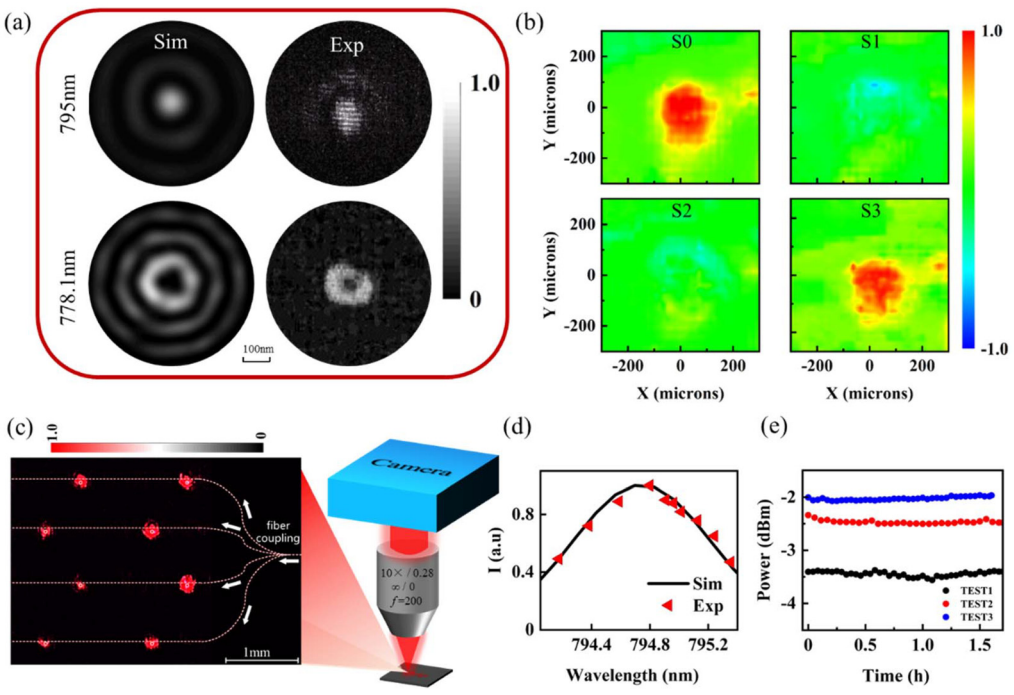

Fig. 3 Experimental results of the SiN microring chip emitter. (a) Comparison between the simulated far-field from a single microring at different wavelengths and the field captured by a CMOS camera; (b) measured Stokes parameter distribution, illustrating a clear visualization of the polarization state of the radiation field; (c) far-field distribution of the microring array and the measurement setup; (d) relationship between λ and normalized radiation intensity; (e) stability of the radiation beam with $l = 3$.

patterns. Fig. 3(c) illustrates the far-field distribution of the microring array chip. Multiple radiation beams are emitted upwards, enhancing light–atom interactions. The variations in intensity distribution stem from manufacturing imperfections in the devices and uncertainties in photon propagation losses on the chip. Fig. 3(d) depicts the relationship between λ and normalized far-field radiation intensity, with the black solid line representing the fitted values and the red triangles indicating experimental measurements. The results demonstrate a close correspondence between the fabricated devices and the simulation, with a mean square error calculated using Lorentz fitting is 0.002962. As the wavelength changes, the far-field radiation intensity also changes, and the maximum radiation intensity occurs at the resonant wavelength. This provides certain advantages for frequency stabilization of pump light for polarized atoms in the future. Stability testing was conducted using the standard deviation method [Fig. 3(e)]. The standard deviation was below 0.1, and the relative standard deviation (RSD) was −2.445, indicating good stability of the radiation beam. Microring chip emitters offer advantages for chip-scale atomic systems, including pure CPL, tunability, robustness, integration, and ease of fabrication, rendering them suitable for optical path structures.

4. The application of microring emitter

4.1. Numerical modeling of optical pumping at 795 nm

In atomic systems, CPL is frequently employed to polarize alkali metal atoms. These atoms absorb photons at specific wavelengths, inducing transitions between energy levels. Due to the brief lifetimes of their excited states, decoherence occurs through various relaxation mechanisms. When a sufficient buffer gas is present in the atomic vapor cell under CPL, the diffusion constant is incorporated into the Bloch equations. The electronic (P_e) and nuclear (P_n) polarization rates are then described by the following eqn (5):[28]

$$\begin{aligned}\frac{\partial P_e}{\partial t} &= \gamma_e P_e \times \boldsymbol{B} + D_e \nabla^2 P_e + R_{op}(s\hat{z} - P_e) - R_{rel} P_e \\ \frac{\partial P_n}{\partial t} &= \gamma_n P_n \times \boldsymbol{B} + D_n \nabla^2 P_n + R_{se}(P_e - P_n) - \Gamma P_n\end{aligned} \tag{5}$$

Here, R_{op}, R_{rel}, R_{se}, and R_n denote the optical pumping rate, the alkali metal spin relaxation rate, the nuclear spin exchange relaxation rate, and the total relaxation rate, respectively. γ_e and γ_n represent the gyromagnetic ratios of free electrons and nuclei, respectively. D_e and D_n signify the diffusion coefficients of alkali metal atoms and noble gases, respectively, which are dependent on the cell temperature and pressure. The CPL polarizes the Rb atoms, which subsequently precess under an external magnetic field $\boldsymbol{B}$. Any process that disrupts the coherence of this precession results in spin relaxation. The microring chip emits RHCP along the z-axis into the cell, and the Rb atoms attenuate the incident light along this axis, as described by eqn (6):

$$\frac{\partial R_{op}(z)}{\partial t} = n_{Rb}\sigma_p R_{op}(z)(1 - sP_e) \tag{6}$$

where n_{Rb} represents the temperature-dependent number density of Rb atoms in the cell, and σ_p denotes the photon absorption cross-section. The optical pumping rate varies with the incident light intensity according to $R_{op} = \sigma_p I_p/(h\nu S_p)$, where I_p and S_p represent the laser power and the beam area, respectively. When the lens fiber and the chip have the optimal coupling efficiency, based on the measured radiation field, the microring's maximum output power is approximately 0.4 mW, with a divergence angle of 4°. The beam radius at the cell entrance measures 0.5 mm. The intensity distribution of the incident light field is expressed by the following eqn (7):

$$I(x,y) = I_p \exp\left(-2\frac{(x-x_0)^2 + (y-y_0)^2}{r^2}\right) \tag{7}$$

Utilizing eqn (5)–(7), we calculated the polarization of atoms on the microring chip. Fig. 4(a) illustrates the distribution of P_e and P_n at the cell center when $s = 1$. The chip incident light power is lower than that of a single beam, resulting in an overall polarization reduction of approximately 20%. Fig. 4(b) depicts P_e and P_n at different propagation distances z within the cell. The microring generates a more uniform polarization of electrons and nucleons with a smaller attenuation gradient compared to a single beam, enhancing overall polarization uniformity by roughly 13%. According to Fig. 4(a) and (b), it can be seen that as the light emitted by the micro ring propagates in the cell, the polarization gradually decreases. The distribution of transverse electron polarization is measured using the Faraday effect in the cell. By comparing the laser polarization before and after it passes through the cell, P_x within the laser detection range can be determined. When utilizing the D1 line of the Rb atom, transitions associated with the D2 line can be disregarded due to their frequency difference of several THz. θ is expressed by the following eqn (8):[29]

$$\theta = \frac{1}{4} n_{Rb} r_e c l f_{D1} P_x \frac{\Delta\nu}{(\Delta\nu)^2 + (\Gamma_L/2)^2} \tag{8}$$

where $r_e = 6.626 \times 10^{-34}$ J S is the electron radius, l is the length of the cell, f_{D1} is the oscillation strength of the D1 line, Γ_L represents pressure broadening, and P_x is the projection of P_n on the x-axis. When pressure and temperature are fixed, P_e remains the sole variable. By applying a modulation field along the x-axis, the electron magnetic moment can be tilted into the xy plane, enabling measurements using linearly polarized light. Fig. 4(c) illustrates the calculated optical rotation angle and signal. As the detection light frequency approaches the ^{87}Rb atomic transition frequency, θ approaches zero, rendering the system output undetectable. Selecting an appropriate laser frequency is crucial for θ detection. As the frequency shifts, the signal exhibits two peaks due to the output being

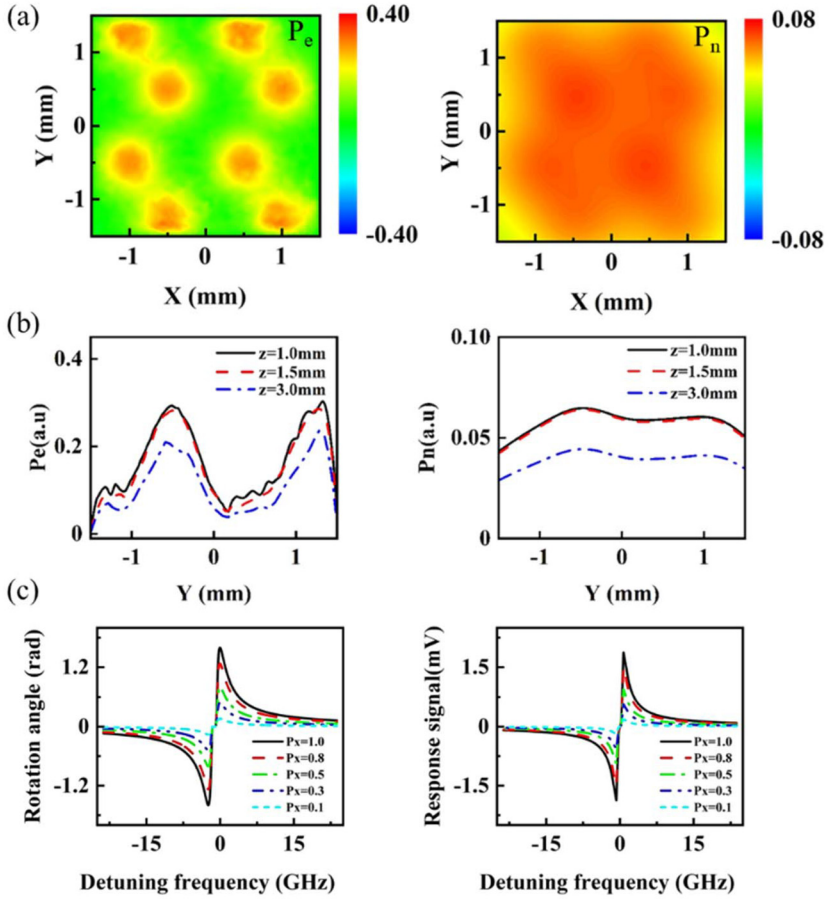

Fig. 4 The electron and nuclear polarizability under the microring chip pumping form. (a) Distribution of P_e and P_n at the center of the 3 mm cell for s = +1; (b) the distribution of P_e and P_n at different propagation distances z positions at the dotted line; (c) correlation between $\Delta\nu$ and P_x in relation to the optical rotation angle and response signal.

an odd function of $\Delta\nu$. These findings indicate that the microring emitter radiates RHCP, achieving optical path miniaturization. The microring chip polarizes electrons and nuclei more uniformly, enhancing the polarization uniformity within the cell and potentially enhancing system integration and reliability.

4.2. Numerical modeling of atomic frequency stabilization at 778.1 nm

Two-photon spectroscopy plays a crucial role in high-resolution spectral analysis within atomic and molecular physics. The Rb two-photon spectrum, characterized by a natural linewidth of 667 kHz,[10] exhibits sensitivity to broadening mechanisms and is frequently utilized in optical frequency standards.[21] In the field of quantum metrology, optical atomic clocks offer precise timekeeping capabilities.[23] By coupling the light from an external 778.1 nm laser into a planar waveguide through a single-mode fiber, the stable vortex beam can be radiated into free space after being transmitted through the waveguide and passing through the micro ring structure. The on-chip structure provides a highly stable environment for light propagation, reducing fluctuations in the light source frequency. Furthermore, the integrated design simplifies the system architecture, reducing reliance on complex components such as modulators and frequency doublers. The energy level transition demonstrates a strong excitation rate for the $5^2S_{1/2} \rightarrow 5^2D_{5/2}$ two-photon transition, with a minimal 2 nm detuning from the intermediate $5^2P_{3/2}$ state, yielding a signal-to-noise ratio (SNR) of approximately 450.[30] This enhancement contributes to improved signal strength, stability, and accuracy in frequency standard applications.[23,31] The coupled wave eqn (9) in 2PA theory delineates the variation of pump light intensity along the z-axis within the cell.[32]

$$\frac{dI_1(\nu_1,z)}{dz} = -\frac{3(2\pi\nu_1)}{n_1 n_2}\mu_0 I_1(\nu_1,z)I_2(\nu_2,z)\mathrm{Im}[\chi^{(3)}(-\nu_{UV},\nu_1,\nu_2,-\nu_{IR})] \quad (9)$$

Here, ν_1 and ν_2 represent the incident laser frequencies, with the wave number is $k_1 = 2\pi/\nu_1$. ν_{UV} and ν_{IR} denote the blue light frequency (714.0 THz) and mid-infrared light frequency (57.3 THz), respectively, as shown in Fig. 1(c). c represents the speed of light, and the vacuum magnetic flux μ_0 is $4\pi \times 10^{-7}$ H m^{-1}. The function Im[$\chi^{(3)}$] represents the imaginary part of the third-order polarizability, which is associated with the

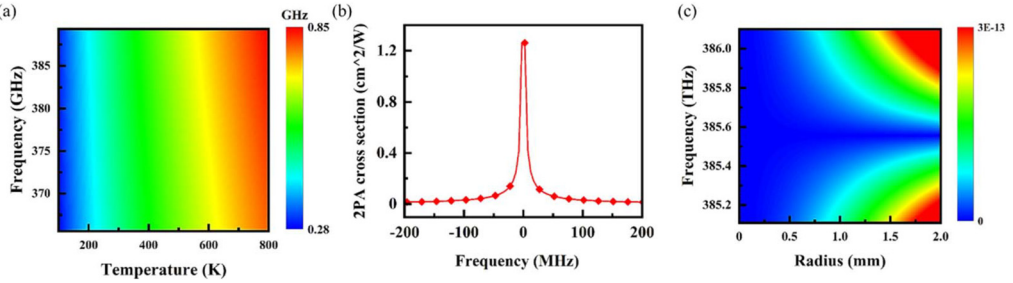

Fig. 5 (a) Energy level Doppler half-width as a function of temperature and incident laser frequency; (b) relationship between the 2PA cross-section and the incident wavelength for the Rb atom transition spectrum of $5^2S_{1/2} \rightarrow 5^2D_{5/2}$; (c) correlation between beam R, pumping light frequency, and stability variation.

absorption cross-section. The subsequent 2PA cross-section σ is derived from the coupled wave equation:[33]

$$\sigma(\nu_1,\nu_2) = \frac{3(2\pi\nu_1)^2}{{k_1}^2 c^2 n_{\mathrm{Rb}}}\mu_0 \mathrm{Im}[\chi^{(3)}(-\nu_{\mathrm{UV}},\nu_1,\nu_2,-\nu_{\mathrm{IR}})] \times S_{\mathrm{FF''}} \times f_{\mathrm{iso}} \times f_{\mathrm{F}} \quad (10)$$

where f_{iso} represents the relative proportion of each stable isotope under natural conditions, with f_{iso} (^{87}Rb) = 27.8%; f_{F} denotes the distribution ratio of particles above and below the $5^2S_{1/2}$ ground state energy level. Eqn (10) demonstrates that σ is directly proportional to the laser frequency and the Im[$\chi^{(3)}$] of the medium. $S_{\mathrm{FF''}}$ denotes the relative hyperfine intensity, reflecting the relative probability of transitions between hyperfine states. The specific expression is as follows:[32]

$$S_{\mathrm{FF''}} = (2F''+1)(2J+1)\begin{Bmatrix} J & J'' & 1 \\ F'' & F & 1 \end{Bmatrix}^2 \quad (11)$$

Utilizing eqn (9)–(11), the cross-section σ of Rb atoms can be calculated, considering a linewidth of approximately 1.218 GHz. Fig. 5(a) illustrates the relationship between the Doppler width, temperature, and laser frequency. Fig. 5(b) demonstrates the variation of σ with wavelength for the $5^2S_{1/2} \rightarrow 5^2D_{5/2}$ transition, exhibiting a peak value of 1.261 cm^2 W^{-1}. The findings suggest that when the incident light's center frequency approaches the 5D energy level, the $5^2S_{1/2} \rightarrow 5^2D_{5/2}$ transition becomes predominant, resulting in enhanced 2PA efficiency.

Based on our previous measurements, we calculate the short-term frequency stability. For 2PA transitions, the incident light frequency is $\omega_1 = \omega_2$. The Doppler shift induced by atomic motion is expressed as $\Delta\omega = (\omega_1 - \omega_2)v/c$, where v represents the atomic thermal velocity. When $\Delta\omega = 0$, the system experiences no Doppler shift. From the preceding analysis of 2PA, the short-term frequency stability is given by eqn (12):[34]

$$\tau = \frac{1}{2\dfrac{\nu_{\mathrm{p}}}{\Delta\nu}\cdot\dfrac{V_{\mathrm{sig}}}{V_{\mathrm{noi}}}} \quad (12)$$

where V_{sig} and V_{noi} represent the transition spectral line signal and system noise, respectively. V_{sig} is inversely proportional to R, $V_{\mathrm{sig}} \propto I_{\mathrm{P}}/\pi R^2$. According to eqn (12), the 2PA transition natural linewidth of ^{87}Rb atoms (300 kHz) is narrower than the linewidth typically obtained from saturated absorption methods, rendering it more suitable for enhancing stability. As illustrated in Fig. 5(c), decreasing the power density of the incident light substantially improves system stability. High power density induces strong thermal and nonlinear effects, which negatively impact stability. Increasing the beam radius reduces the power density, mitigating these effects and enhancing short-term stability. Furthermore, higher frequencies result in Doppler broadening, where relative motion within the system expands the light spectrum. This amplifies noise, induces frequency instability, and diminishes precision. Consequently, regulating the incident light power and frequency is crucial for system stability. Balancing these factors presents a significant challenge in designing compact, high-precision laser systems. In comparison to traditional optical components, the proposed device facilitates a more compact design for applications such as atomic system frequency stabilization, promoting system miniaturization and high integration.

5. Conclusions

With the advancement of atomic system measurement technology, the demand for high-performance light sources continues to grow. Pure CPL, highly stable, and miniaturized sources are particularly crucial in quantum information processing, precision measurement, and quantum sensing.[35] This study presents a SiN chip emitter based on microring etched grating structures, offering high integration, excellent robustness, and simplified fabrication. Simulation and experimental results demonstrate that the chip can generate circularly polarized and vortex light at specific wavelengths, providing novel techniques for precise atomic system measurements. At 795 nm, the chip emits pure and stable CPL, meeting the requirements for atomic system measurements and enhancing atomic polarization uniformity by approximately 13%. At 778.1 nm, it consistently generates l = 3 vortex light, which is essential for stabilizing frequency-locked laser output and

maintaining low beam divergence. As quantum light sources and integrated optics continue to advance, the microring chip emitter could play a pivotal role in high-precision optics and quantum communication, offering reliable optical support for the commercialization of quantum technologies.

Author contributions

X. Q. M. and Z. C. conceived and designed the idea. X. Q. M. and Y. T. X. designed and characterized the microring with assistance from Y. T., J. S., X. R. S. and X. L. W. helped build the test system. X. Q. M. performed the test and analyzed the data. X. Q. M. and Z. C. wrote the manuscript with input from all authors.

Conflicts of interest

The authors declare no conflict of interest.

Data availability

The data that support the findings of this study are available from the corresponding author upon reasonable request.

Theoretical model of radiation beam, optimization of microring parameters, Stokes parameter calculation method, the image of the experimental setup and far-field beam distribution. See DOI: **https://doi.org/10.1039/d5nr02285a**

Appendix: Experimental setup

A single-mode lens fiber (PMF-FC/APC, Zhongshan Meisu Technology Co., Ltd) with a mode-field diameter of 2.8 μm was mounted on a five-axis displacement table, enabling precise adjustment of its position relative to the incident waveguide on the chip. UniQuanta's distributed Bragg reflection (DBR) semiconductor narrow-linewidth laser were employed to generate LPL at a central wavelength of 795 ± 0.01 nm through careful modulation of the laser drive power supply. This laser functioned as the pump source for the single-mode lens fiber, enhancing mode matching with the chip-edge inverted-taper coupler. A high-precision setup consisting of a 12.5× zoom objective (AP-ZMLP-12X-FF-COAX, Apico) and a CMOS camera (AP-MV-UH1080, Apico) facilitated the coupling of the lensed fiber to the chip end face and allowed visualization of the radiated beam field distributions. The DBR laser wavelength was subsequently tuned, focused, and collimated using a 10× objective lens (WG181252821, Mitutoyo, Japan), with the optical power measured by a power meter (PM100D, Thorlabs).

Acknowledgements

This research was supported by Beijing Natural Science Foundation under Grant No. 4232071, General Program of National Natural Science Foundation of China under Grant No. 62373028, Zhejiang Provincial Natural Science Foundation of China under Grant No. LZ24F050007.

References

1 D. Budker and M. Romalis, Optical magnetometry, *Nat. Phys.*, 2007, **3**(4), 227–234.
2 H. Korth, K. Strohbehn, F. Tejada, *et al.*, Miniature atomic scalar magnetometer for space based on the rubidium isotope ^{87}Rb, *J. Geophys. Res.: Space Phys.*, 2016, **121**(8), 7870–7880.
3 D. Meyer and M. Larsen, Nuclear magnetic resonance gyro for inertial navigation, *Gyroscopy Navig.*, 2014, **5**(2), 75–82.
4 Z. L. Newman, V. Maurice, T. Drake, *et al.*, Architecture for the photonic integration of an optical atomic clock, *Optica*, 2019, **6**(5), 680–685.
5 D. J. Blumenthal, R. Heideman, D. Geuzebroek, *et al.*, Silicon nitride in silicon photonics, *Proc. IEEE*, 2018, **106**(12), 2209–2231.
6 J. Kitching, Chip-scale atomic devices, *Appl. Phys. Rev.*, 2018, **5**(3), 031302.
7 D. X. Sun, D. L. Zhang and F. Bi, Silicon-based microring resonant cavity applied to integrated optical gyroscope sensitive unit, *Laser Optoelectron. Prog.*, 2022, **59**(15), 1513001.
8 S. Corsetti, A. Hattori and R. Swint, *et al.*, Integrated polarization-diverse grating emitters for trapped-ion quantum systems, in *Laser Science*, Optica Publishing Group, 2023, pp. JTu7A.3.
9 R. J. Niffenegger, J. Stuart, C. Sorace-Agaskar, *et al.*, Integrated multi-wavelength control of an ion qubit, *Nature*, 2020, **586**(7830), 538–542.
10 M. T. Hummon, S. Kang, D. G. Bopp, *et al.*, Photonic chip for laser stabilization to an atomic vapor with 10^{-11} instability, *Optica*, 2018, **5**(4), 443–449.
11 Y. Livneh, A. Yaacobi and M. Orenstein, Two-dimensional quasi periodic structures for large-scale light out-coupling with amplitude, phase and polarization control, *Opt. Express*, 2022, **30**(6), 8425–8435.
12 G. D. Martinez, C. Li, *et al.*, A chip-scale atomic beam clock, *Nat. Commun.*, 2023, **14**(1), 3501.
13 C. Ropp, D. Maurya, A. Yulaev, *et al.*, Scalable and robust beam shaping using apodized fish-bone grating couplers, *Opt. Express*, 2023, **31**(24), 40792–40802.
14 L. He and M. Li, On-chip synthesis of circularly polarized emission of light with integrated photonic circuits, *Opt. Lett.*, 2014, **39**(9), 2553–2556.
15 X. Guo, Y. Ding, X. Chen, *et al.*, Molding free-space light with guided wave–driven metasurfaces, *Sci. Adv.*, 2020, **6**(29), eabb4142.
16 Y. Zhang, Z. Li, *et al.*, On–Chip Multidimensional Manipulation of Far–Field Radiation with Guided Wave–Driven Metasurfaces, *Laser Photonics Rev.*, 2023, **17**(9), 2300109.
17 J. Huang, *Waveguide integrated metasurfaces for on-chip vortex beam generation*, University of Southampton, 2024.

18 L. Massai, T. Schatteburg, J. P. Home, *et al.*, Pure circularly polarized light emission from waveguide microring resonators, *Appl. Phys. Lett.*, 2022, **121**(12), 121101.
19 T. L. Nicholson, S. L. Campbell, R. B. Hutson, *et al.*, Systematic evaluation of an atomic clock at 2×10^{-18} total uncertainty, *Nat. Commun.*, 2015, **6**(1), 1–8.
20 D. Xia, C. Yu and L. Kong, The development of micromachined gyroscope structure and circuitry technology, *Sensors*, 2014, **14**(1), 1394–1473.
21 K. W. Martin, G. Phelps, N. D. Lemke, *et al.*, Compact optical atomic clock based on a two-photon transition in rubidium, *Phys. Rev. Appl.*, 2018, **9**(1), 014019.
22 J. Kitching, M. Hummon, W. McGehee, *et al.*, Next-Generation Chip Scale Atomic Clocks, *J. Phys.: Conf. Ser.*, 2024, **2889**(1), 012015.
23 N. D. Zameroski, G. D. Hager, C. J. Erickson, *et al.*, Pressure broadening and frequency shift of the $5S_{1/2} \rightarrow 5D_{5/2}$ and $5S_{1/2} \rightarrow 7S_{1/2}$ two photon transitions in ^{85}Rb by the noble gases and N_2, *J. Phys. B: At., Mol. Opt. Phys.*, 2014, **47**(22), 225205.
24 Y. M. Meng, J. F. Xiang and B. Xu, Frequency stabilization characteristics of ^{87}Rb two-photon transition spectrum, *Chin. Opt. Lett.*, 2023, **50**(23), 2301013.
25 X. Cai, J. Wang, M. J. Strain, *et al.*, Integrated compact optical vortex beam emitters, *Science*, 2012, **338**(6105), 363–366.
26 J. Wang, X. Yang, Y. Li, *et al.*, Optically spatial information selection with hybridly polarized beam in atomic vapor, *Photon. Res.*, 2018, **6**(5), 451–456.
27 Y. Xu, Z. Chai, X. Meng, *et al.*, Silicon Nitride–Photonics–Enabled Optical Pumping for Optically Pumped Magnetometer, *Laser Photon. Rev.*, 2025, **19**(10), 2402292.
28 J. Yuchen, L. Zhanchao, Z. Binquan, *et al.*, Pump beam influence on spin polarization homogeneity in the nuclear magnetic resonance gyroscope, *J. Phys. D: Appl. Phys.*, 2019, **52**(35), 355001.
29 Y. Xu, Y. Xu, J. Sun, *et al.*, Atomic Spin Detection Method Based on Spin–Selective Beam–Splitting Metasurface, *Adv. Opt. Mater.*, 2024, **12**(2), 2301353.
30 F. Nez, F. Biraben, R. Felder, *et al.*, Optical frequency determination of the hyperfine components of the $5S_{,1/2}$-$5D_{3/2}$ two-photon transitions in rubidium, *Opt. Commun.*, 1993, **102**(5–6), 432–438.
31 O. Terra and H. Hussein, An ultra-stable optical frequency standard for telecommunication purposes based upon the $5S_{1/2} \rightarrow 5D_{5/2}$ two-photon transition in Rubidium, *Appl. Phys. B: Lasers Opt.*, 2016, **122**, 1–12.
32 Y. Ji, Y. He, H. Wan, *et al.*, Theoretical modeling and analysis of blue laser characteristics of continuous-wave single-wavelength two-photon pumped Rb-vapor laser, *IEEE J. Quantum Electron.*, 2021, **58**(1), 1–8.
33 H. Yu, F. Chen, Y. He, *et al.*, Theoretical modeling and analysis on the absorption cross section of the two-photon excitation in Rb, *Opt. Express*, 2018, **26**(13), 17254–17263.
34 M. Callejo, A. Mursa, R. Vicarini, *et al.*, Short-term stability of a microcell optical reference based on the Rb atom two-photon transition at 778 nm, *J. Opt. Soc. Am. B*, 2024, **42**(1), 151–159.
35 D. J. Blumenthal, A. Isichenko and N. Chauhan, Enabling photonic integrated 3D magneto-optical traps for quantum sciences and applications, *Opt. Quantum*, 2024, **2**(6), 444–457.